Materials Research. 2024; 27(suppl. 1):e20230578
DOI: https://doi.org/10.1590/1980-5373-MR-2023-0578

Impact of Feedstock Recycling on the Corrosion Resistance of Inconel 625 Processed by L-DED

***Juliane Ribeiro da Cruz*[a,b], *Jurandir Marcos Sá de Sousa*[a], *Henrique Santos Ferreira*[a], *Anselmo Thiesen Junior*[a], *Cláudia E. B. Marino*[c]**

[a]*Instituto SENAI de Inovação em Sistemas de Manufatura, Processamento a Laser e Excelência Operacional, R. Arno Waldemar Döhler, 308, 89218-510, Joinville, SC, Brasil.*
[b]*Universidade de São Paulo, Escola Politécnica, Departamento de Engenharia Mecânica, Av. Prof. Mello Moraes, 2231, 05508-030, São Paulo, SP, Brasil.*
[c]*Universidade Federal do Paraná, Departamento de Engenharia Mecânica, Av. Cel. Francisco H. dos Santos, 230, 81530-001, Curitiba, PR, Brasil.*

Received: December 29, 2023; Revised: May 29, 2024; Accepted: May 29, 2024

The corrosion resistance of Inconel 625 processed by L-DED additive manufacturing using virgin and reused powders was investigated to optimize the cost-effectiveness of the process. Samples were manufactured under a controlled argon atmosphere. Feedstock and samples were characterized by optical and scanning electron microscopy, energy-dispersive X-ray spectroscopy, and rheology analysis. Corrosion resistance was investigated by cyclic polarization and electrochemical impedance spectroscopy in NaCl 3.5% media. Rheology accused a slight decrease in powder flowability with reuse, but no further appreciable powder degradation was observed. Samples developed a dendritic microstructure with Mo- and Nb-rich Laves phase in the interdendritic region. Samples processed with reused powder were found to have a high content of oxides, which accounted for a slightly inferior impedance and reduced the charge transfer resistance by nearly 50%. Specimens had an overall similar cyclic polarization, with the specimen processed with virgin powder having a slightly superior performance, with a 60mV more noble E_{corr} and higher R_p, but similar I_{corr}. Samples presented uniform and pitting corrosion mechanisms, with pits being preferentially located in the Mo-depleted dendritic regions. In summary, the reuse of Inconel 625 powder processed under argon-controlled conditions was not considered to be significantly detrimental to the alloy corrosion resistance.

Keywords: *Ni-superalloys, Corrosion mechanisms, Tafel analysis, Laser processing, Feedstock recycling.*

1. Introduction

Inconel 625 is a nickel Ni-based superalloy with superior mechanical strength and great corrosion resistance, at milder and high-operating temperatures. It is extensively used in high-tech industrial sectors such as aviation, aerospace, nuclear, marine, and petrochemical to produce turbine blades, heat exchangers, valves, and several other parts[1-3]. However, processing Inconel 625 is a complex task due to its high toughness, high abrasiveness, and poor machinability[4-6].

With additive manufacturing (AM) by laser directed energy deposition (L-DED), and laser powder bed fusion (L-PBF), it is possible to produce components with customized geometries on-demand using materials that are challenging to work with[3,7-9]. This work focuses on the L-DED process, which provides the manufacturing and repair of parts ensuring a refined and heterogeneous microstructure through a series of fast heating-cooling cycles that generate high temperature gradient/solidification ratio correlations. With the feasible selection of L-DED parameters and AM manufacturing strategies, it is possible to obtain components free from deleterious defects, with high density and properties compatible with and/or superior to traditional manufacturing methods[2,10]. In this sense, the processing of Inconel 625 parts by AM stands out as a viable alternative.

Despite the benefits, Inconel 625 has the limitations of forming potentially deleterious phases, with the Laves phase being the most commonly found. It is an intermetallic compound with a hexagonal structure, rich in Nb and Mo $Ni_2(Mo, Nb)$, normally precipitated at grain boundaries. Besides, the Laves phase is hard and brittle, providing sites for nucleation and propagation of cracks[11]. During solidification, the initial reaction of the primary liquid transforming into austenite provides supersaturation of Mo and Nb to the interdendritic regions and grain boundaries. This kinetics is encouraged by the very high melting points of these elements. In this context, the Ni-rich dendritic matrix is depleted in these elements, reducing corrosion resistance, through the establishment of preferential sites for the action of corrosive mechanisms, such as pits[4]. The formation of a Cr_2O_3 passivating film on the Inconel 625 surface is mainly responsible for its attractive corrosion resistance[12]. However,

*e-mail: juliane.rcruz@usp.br

during AM L-DED manufacturing, fast cooling generates segregation at grain boundaries, material undergoes intense microstructure and surface modification, which can impair this property. Precipitation of carbides and Laves phases generates a sensitization phenomenon, depleting the matrix region in Cr, thus decreasing corrosion performance[13].

Once manufactured, AM L-DED Inconel 625 components can be subjected to a heat-treatment route consisting of annealing and, sometimes, aging. Different times (e.g. 60-120 min) and temperatures (e.g. 800-1150 °C) are reported. The objective is to provide residual stress relief, recrystallization, mitigate segregation, and improve the mechanical properties and corrosion resistance[14,15].

To enhance the sustainability and cost-effectiveness of AM L-DED process, powder reuse has emerged as a common approach. AM, defined as a set of emerging processes, still presents a high cost, with a significant portion of this attributed to the metallic powder acquisition, which is manufactured using high-added-value processes, such as gas and plasma atomization[16]. In the literature, there are still few works in this regard. Gutjahr's doctoral thesis (note: original document in Portuguese, Brazil) presents a complete discussion of the effects of eight cycles of reuse of a 316L austenitic stainless steel powder on standardized specimens manufactured by AM L-DED process. The author analyzed aspects of microstructure, and mechanical performance of hardness, tensile strength, and Charpy impact. As general conclusions, it was observed that there was no significant difference in microstructure and mechanical performance along with the multiple cycles. The efficient control of oxygen (O_2) level using an Argon-rich controlled atmosphere throughout all stages of feedstock handling, manufacturing, and post-processes was the main justification indicated for achieving satisfactory performance[17]. By producing AM L-DED samples in five reuse cycles, Renderos et al.[18] assessed the degradation of Ni-based superalloy Inconel 718. Throughout the reuse cycles, the authors found no appreciable variations in the chemical composition, microstructure, or mechanical tensile performance[19].

Based on the literature, it is feasible to infer that there is a trend for powder reuse to not adversely affect the material performance, if caution is used throughout the manufacturing process, especially while handling the feedstock. It is advised to employ a controlled atmosphere during the process to minimize the negative effects of oxygen and other atmospheric pollutants on the material. Metal powder reuse is a relatively common AM practice in the laser powder bed fusion (L-PBF) process. However, there is still a lack of studies on the effects of these practices in different materials processed by L-DED. Attention is drawn to the case of Inconel 625, which is a high-cost material already widely used in high-tech industrial sectors. For example, the impact of feedstock reuse on the corrosion performance of AM L-DED Inconel 625 parts is not yet fully understood.

In this context, the present work shows the impact of feedstock reuse on the corrosion performance of AM L-DED Inconel 625 parts in the as-built and heat-treated states. This work brings a technological contribution showing that the reuse of powder processed by AM L-DED under an inert gas-controlled atmosphere does not jeopardize the corrosion resistance of Inconel 625. Besides, this research also contributes towards a better comprehension of the corrosion mechanisms of Inconel 625 powder and parts, when processed by AM L-DED.

2. Materials and Methods

Hot-rolled and milled AISI 316 stainless steel (250×50×15 mm) plates were used as substrate. A gas-atomized Ni-based Inconel 625 virgin powder with 53-150 µm particle size range was used as feedstock. Table 1 shows their chemical composition.

L-DED system used was the 5-axis RPMI 535® from RPM Innovations Inc., which is capable of processing in a controlled atmosphere composed of Argon gas, keeping an oxygen (O_2) content below 10 ppm. It is coupled to a continuous wave (CW) Ytterbium (Yb) doped fiber laser source with 3000 W (YLS-3000) nominal power, 1064 nm wavelength (λ), Beam Parameter Product (BPP = 10.0), and Beam Parameter Quality ($M^2 = 29.7$) from IPG Photonics®.

Figure 1 presents a schematic illustration of the steps used in the specimens manufacturing of this work. For the present study, a set of samples (25×25×25 mm cubes) were manufactured by AM L-DED under an Argon-controlled atmosphere, with an O_2 content below 5 ppm, using the parameters shown in Table 2, that were previously optimized for mechanical integrity following a standardized design of experiment (composed by experimental and analytical stages of single beads, single layers, and multilayer samples) as that applied by Thiesen[20]. A slicing strategy with a 45° rotation between layers was used during manufacturing. A layer-by-layer relay between cube samples was employed aiming to mitigate excessive heat input.

The processing setup (power nozzle and process parameters) was tuned for mechanical integrity assurance (free from cracks and lack of fusion), and low deposition efficiency, which was of about 15%. It is estimated that, from the total amount of powder provided for manufacturing (100%), 5% is lost in dead moves, 2% because of powder dropping off the build platform, 1% during the sieving process, and 1% along with storage handling. This way, even after parametrization (that also consumes a certain amount of powder), a great part of the initially fed feedstock would still be available for reuse. After manufacturing, the powder remaining on the build platform was collected and stored.

Table 1. Chemical composition of the substrate and feedstock materials.

	Chemical Composition							
Element (wt.%)	Fe	Ni	Cr	Mo	Nb	Mn	Si	C
AISI 316 Substrate	Bal.	0.7	13.5	-	-	1.0	1.0	0.15
Inconel 625 Powder	0.5	Bal.	21.1	8.3	5.0	0.4	0.5	0.01

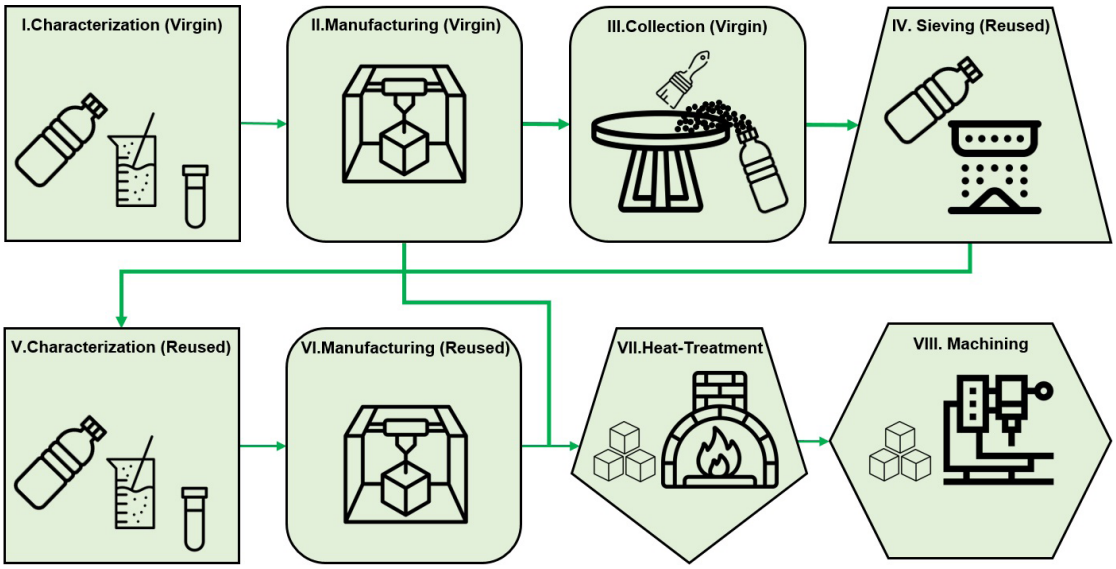

Figure 1. Experimental steps performed during powder handling, powder characterization, and AM L-DED manufacturing.

Table 2. AM L-DED optimized parameters.

AM L-DED Parameter	Value
Spot Size (Ø, mm)	1.78
Powder Feedrate (F, g/min)	15
Laser Power (P, W)	550
Travel Speed (S, mm/min)	457
Hatch Spacing (HS, mm)	1.0
Layer Height (mm)	0.64

Bottles of virgin and reused powders were kept inside a glove box filled with argon (MBRAUN UNIlab) that maintains the internal O_2-content below 10 ppm. The reused powder sieving process was conducted at the VIBROWEST sieving station, which runs in a controlled atmosphere by Argon with an O_2-content below 10 ppm. In this procedure, a #100 Mesh sieve was used, which prevents the passage of particles larger than 150 µm. After sieving, samples of virgin and reused powders were collected according to recommendations of ASTM B215 (Standard Practices For Sampling Metal Powders)[21]. The morphology and microstructure of powder samples were characterized by SEM imaging using a ZEISS SUPRA 55 VP equipment and by optical microscopy using a ZEISS AXIO IMAGER 2. Rheology analyses were performed using a FREEMAN TECHNOLOGY FT-4 equipment. Aeration, stability, and variation flow rate tests were carried out to determine the feedstock's Aeration Rate (AR), Basic Fluidity Energy (BFE), Flux Rate Index (FRI), Stabilization Index (SI), and Specific Energy (SE). For every rheological test, at least three repetitions were performed. SEM imaging was performed for morphology analysis of the virgin and reused powders.

The sieved powder was then used to produce samples using the same parameters employing 100% of the reused powder. Once manufactured, both samples were subjected to a stress relief heat-treatment in the ambient atmosphere performed at 900 °C for 120 min followed by in-furnace cooling. After that, samples were machined off the substrate by wire electron discharge and milling for finishing.

Samples manufactured were cross-sectioned in 25*25*5 mm slices and subjected to conventional metallographic preparation composed by grinding with SiC papers from #80 to #1200 mesh, and polishing in 1 µm diamond solid-solution suspension. To reveal the underlying microstructure, samples were etched by immersion in fresh Acqua Regia solution (50 ml HCl + 50 ml H_20 + 3 ml HNO_3). Quantitative microscopy analysis was used to estimate the fraction of second-phase precipitates. As the microstructure of the specimens is relatively heterogeneous, the location where the images would be captured was standardized, to allow for a direct comparison. High magnification optical microscopy images were captured in the middle of the bead (polygonal grains region), in at least seven different regions for each sample. Then, ImageJ software was used to quantify the fraction of second phases (in area %), and OriginLab software was employed to perform a one-way ANOVA and Tukey test, for means comparison, using a significance level of 0.05. The optical microscope used in these investigations was a ZEISS AXIO IMAGER 2.

An illustration of the characterization steps is presented in Figure 2. The initial microstructure was investigated by optical and scanning electron microscopy and the chemical composition by energy dispersive X-ray spectroscopy (EDS) analysis. Back scattered electron (BSE) imaging mode was used to highlight chemical composition differences, while secondary electrons (SE) imaging was used to capture images under optimum topographical resolution. The scanning electron microscope used for these analyses was a ZEISS SUPRA 55 VP.

Corrosion test was performed in a naturally aerated NaCl 3.5% solution. Before the corrosion tests, samples were ultrasonically cleaned with water, alcohol, and acetone, and stored at dry ambient conditions for at least seven 7 days to ensure surface stabilization and natural passivation[22]. Cyclic

polarization (CP) and electrochemical impedance spectroscopy tests were performed using a three-electrode electrochemical cell (Potentiostat Versastat4, Princeton Allied Research), with a platinum foil as counter-electrode and a saturated calomel electrode as the reference electrode (SCE). CP tests were carried out from -150 mV vs OCP to 1.2V vs SCE using scan rates of 5 mV/s. Electrochemical analysis results were normalized by the working electrode area, that was approximately 0.2 cm^2 for all specimens. To attest the repeatability of the results, tests were carried out as duplicates. The results exhibited good repeatability, and the average values and standard deviation are presented. After the polarization tests, the corrosion mechanism was assessed by OM, as illustrated in the Figure 2 scheme. Electrochemical impedance spectroscopy was recorded at a 7-point per decade rate, under a stable OCP, with a voltage amplitude of ± 10 mV RMS and within the frequency range of 100 kHz and 0.1 Hz. Results were fitted using the ZView software.

3. Results and Discussion

3.1. Morphology of virgin and reused Inconel 625 powder

The SEM aspects of Inconel 625 virgin and reused particle's top surface is shown in Figure 3. Although it was

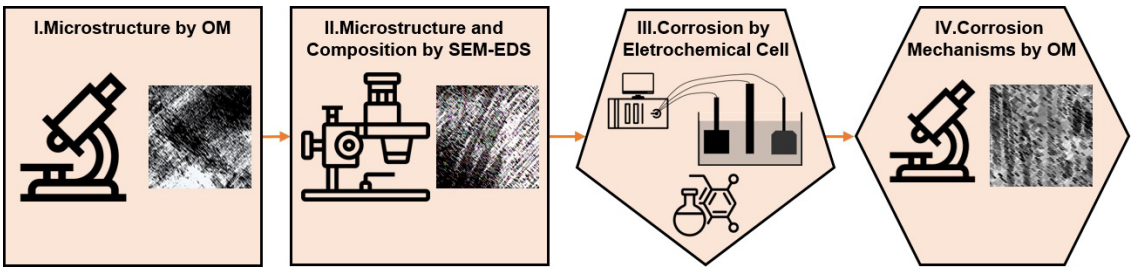

Figure 2. Characterization steps performed in the L-DED samples manufactured by virgin and reused Inconel 625 powder - (I) Optical microscopy analysis, (II) SEM/EDS analysis, (III) Cyclic polarization and electrochemical impedance spectroscopy analysis and (IV) Microscopy analysis for the investigation of the corrosion mechanism.

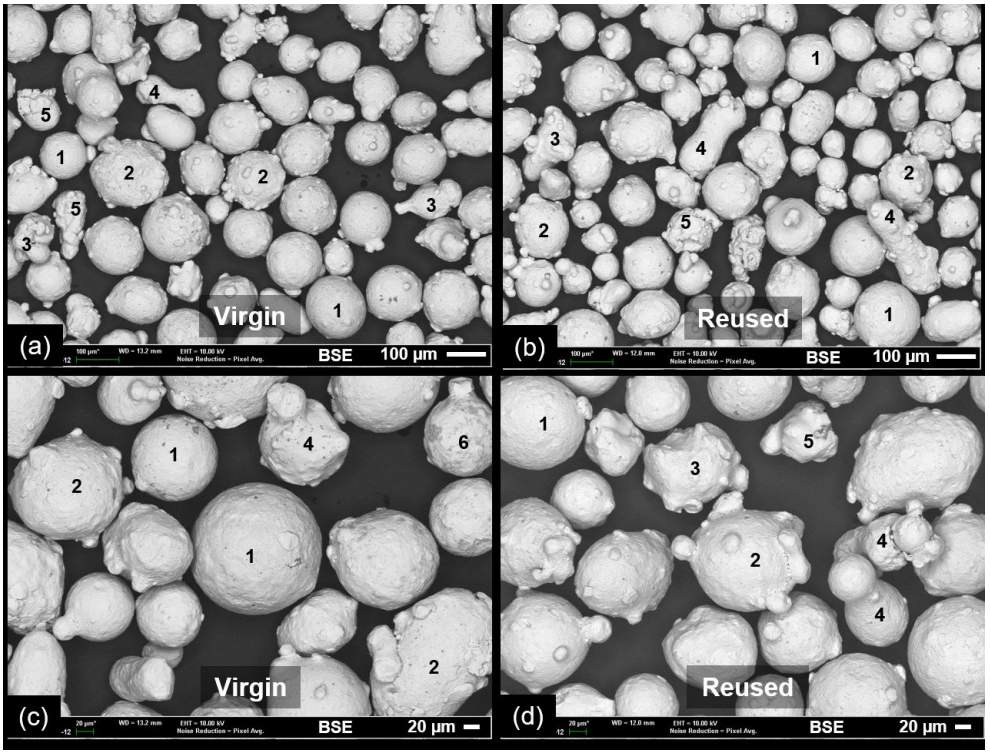

Figure 3. SEM images showing the top surface aspect of the virgin and reused Inconel 625 powder in (a, b) lower and (c, d) higher magnification. No significant difference was observed from one power to the other. Types of particles observed: (1) spherical, (2) with satellites, (3) irregular, (4) agglomeration, (5) remolten, and (6) oxidized.

not possible to detect significant differences between the powders only by SEM analysis, different types of particles present in both powders were mapped out and are shown in Figure 4. Feedstocks were mainly composed of spherical particles (Figure 4a), and round particles with smaller satellite particles attached to them (Figure 4b). In a lower frequency, other types of particles were also seen, including irregular-shaped particles, agglomerated particles, remolten particles, and oxidized particles. Agglomerated particles are the ones that were not fully separated or ended up being attached during the atomization or L-DED processing stage[23].

Remolten particles were found to have a very characteristic topological and cross-sectional aspect, as seen in Figure 5. It is possible to see that, after etching, a white halo is formed around the remolten particles (Figure 5a). This type of particle was seen in both the virgin and reused feedstock. In the case of virgin powder, this indicates that the remelting was caused by the atomization process only. In the case of the reused powder, on the other hand, a similar effect could also be caused by the laser irradiation. SEM analysis under higher magnification reveals that this outermost layer has very refined microstructure, with a solidification mode that shifts from planar to cellular, to columnar dendritic, resembling the aspect of welding molten zones (please see figure 8.5 of the book "Welding Metallurgy"[24]). EDS analysis of remolten particles shown in Figure 6 confirmed that the chemical composition of the outermost unattached layer is the same as that found in the core of the particle. Either by microstructure refinement or by solubilization of precipitates, resistance to etching of the remolten layer (lighter region in Figure 5a) suggests that this region has a higher corrosion resistance than the core of the particle. In this region, the roughness was increased by corrosion during the etching, whereas the roughness of the outermost layer remains flat enough to reflect the light in optical microscopy analysis, like the polished samples (Figure 5a).

Pre-existing Al and Si-oxides were found on the top surface (Figure 4f) and in the core of feedstock particles (Figure 7), in both the virgin and reused powders, which

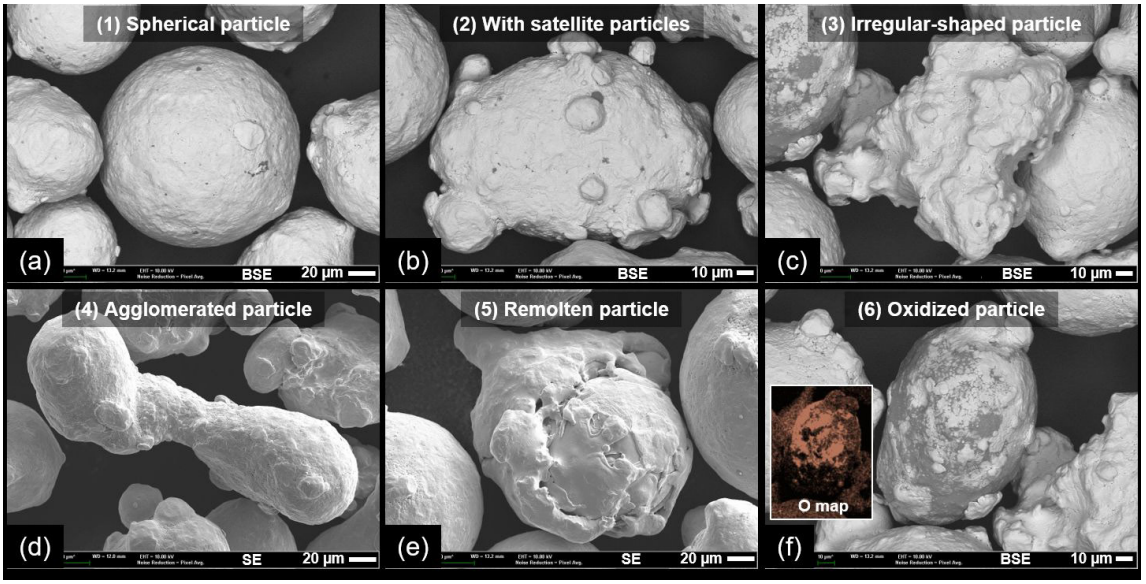

Figure 4. High magnification SEM images showing the types of particles observed in both the virgin and reused Inconel 625 powder: (a) spherical, (b) with satellites, (c) irregular, (d) agglomeration, (e) remolten, and (f) oxidized.

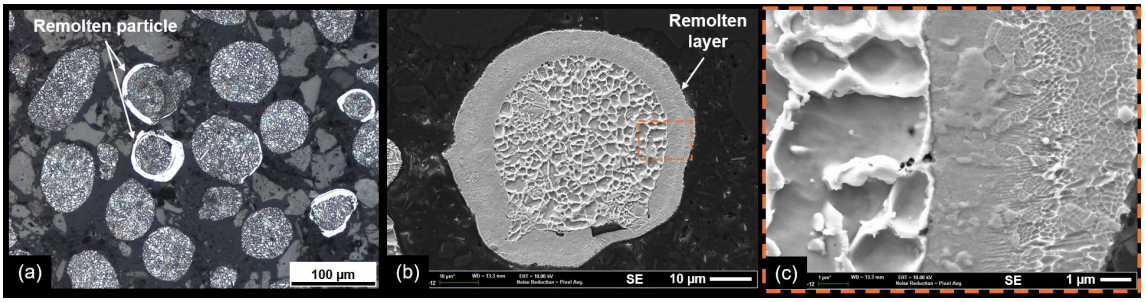

Figure 5. Cross-section of virgin Inconel 625 powder showing (a) optical microstructure of particles with a halo after etching associated with (b) SEM illustrating the remelting of the outermost surface of the particles during the atomization process, (c) a typical fast solidification structure was observed, with microstructure refining accounting for superior resistance to the chemical etching (aqua regia).

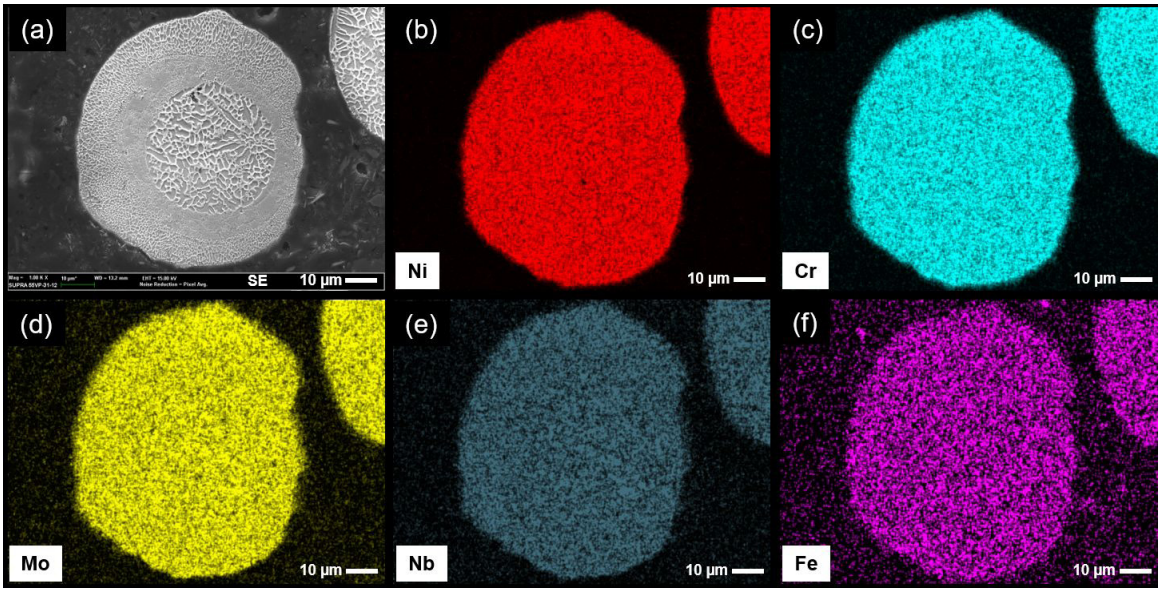

Figure 6. Chemical composition mapping of the cross-section of a remolten particle of Inconel 625 powder (a) showing that the halo has the same chemical composition of the particle core, and highlighting the contents of (b) Ni, (c) Cr, (d) Mo, (e) Nb, and (f) Fe.

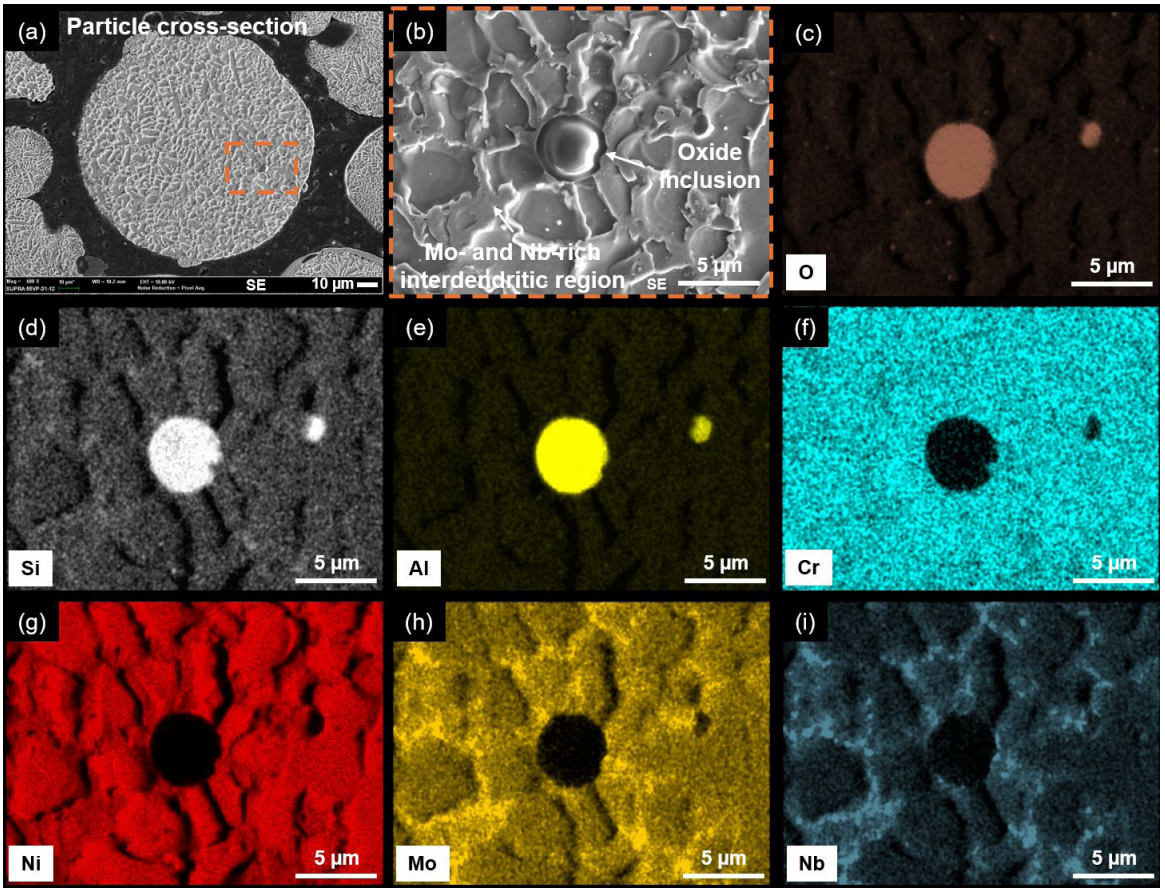

Figure 7. Cross-section of the Inconel 625 powder (a) showing the pre-existence of (b) oxide inclusion in the virgin condition, with high-contents of (c) O, (d) Si, and (e) Al, likely due to contamination during earlier stages of powder manufacturing. The elements (f) Cr, and (g) Ni did not exhibit significant variations. The Interdendritic regions were enriched in (h) Mo, and (i) Nb.

correspond to alloy impurities or contaminations during the atomization process. This is corroborated by the chemical composition shown in Table 1 which does not contain Al. As the alloy contains minor additions of Si (0.5%), it is not possible to know whether the Si-content in the oxides comes from the alloy itself, or extraneous contamination. These Al-rich oxides can also be seen embedded in the remolten layer, as shown in Figure 8.

It is a complex and impractical (costly and time-consuming) task to quantify the amount of these types of particles in each powder (virgin and reused). To avoid excessive cost and labor, ASTM B215 provides recommendations on standard practices for sampling metal powders that used in this study. It is widely known that irregular and agglomerated particles contribute to a decrease the powder flowability, whereas spherical particles flow easily with minimum energy. Processing becomes extremely challenging when irregular powders are used, particularly because of rheological constraints. In the laser powder bed fusion (L-PBF) additive manufacturing process, these characteristics affect the homogeneity of the powder bed. This is a considerably more critical issue in the L-DED technique because the powder must travel through hoses from the storage hoppers to the build platform. Providing a uniform powder and laser beam simultaneously during manufacturing is challenging. In this sense, the entire process and its outcomes may be jeopardized[23,25-27]. For this reason, a rheology analysis of the virgin and reused powders was carried out and is discussed in the following section.

3.2. Morphology impact on rheology of virgin and reused Inconel 625 powder

Results of the rheology analyses carried out in this work (Stability and Variation Flow Rate, and Aeration) are presented in Table 3. Results indicate that the aeration rate (AR), flux rate index (FRI), and stabilization rate (SR) were not significantly affected by the reuse. In contrast, the basic fluidity energy (BFE) and the specific energy (SE) were. The energy required to make the material flow is known to be affected by phenomena such as friction, media conditions, and particle agglomerations[28].

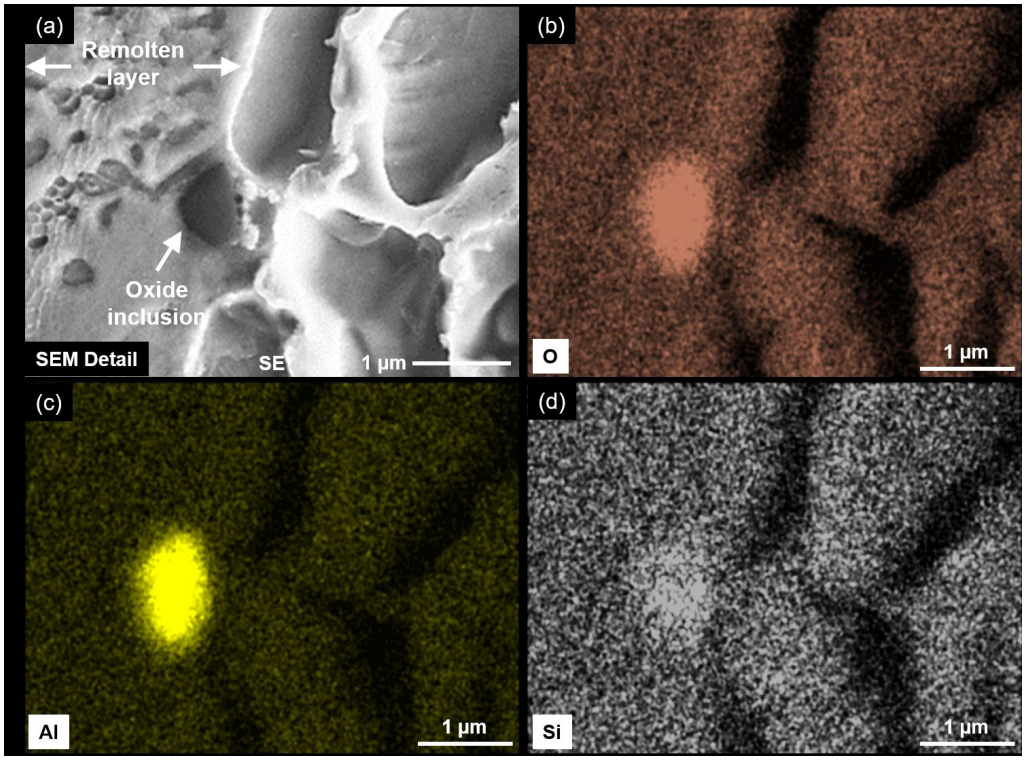

Figure 8. SEM detail of a (a) remolten layer of the reused Inconel 625 powder, with Al- and Si-rich oxide inclusions embedded inside. EDS images point to high-contents of (b) O, (c) Al, and (d) Si.

Table 3. Rheological behavior of Inconel 625 powders under investigation, showing significantly higher energy for powder flowability in the reused powder associated with particle agglomeration.

Powder Condition	BFE (mJ)	SE (mJ/g)	FRI	SI	AR
Virgin	222 ± 38	1.25 ± 0.13	1.09 ± 0.04	1.03 ± 0.12	1.19 ± 0.02
Reused 1x	293 ± 04	1.63 ± 0.03	1.09 ± 0.06	1.01 ± 0.02	1.25 ± 0.03

Footnote: BFE - Basic Fluidity Energy, SE - Specific Energy, FRI - Flux Rate Index, SI - Stabilization Index, AR - Aeration Rate.

For the reused powder, the increase in the BFE (which is the energy measured in a cycle with the blade in a downward motion), indicates a greater flowability difficulty under compression, which could be related to differences in particle morphology. This suggests that the reused feedstock contains a higher number of particles that differ from the spherical shape shown in Figure 4a, which is coherent considering that the particle's exposure to the laser beam could easily lead to the particle's agglomeration and remelting, whose protuberances are expected to provide more flow resistance and powder compressibility[27-29].

SE parameters were also significantly higher for the reused powder, approximately 23%. This parameter measures the opposite effect of BFE, which is the energy consumed in the upward blade movement. SE is related to the shear effort and cohesion between powder particles, without the compression portion associated with BFE. Like the BFE, the greater amount of energy to move the blade upwards also indicates a higher degree of friction and entanglement in between the particles that could be related to a high number of agglomerates. Still, materials with SE < 5 are considered to have low cohesion[28]. In this context, it is safe to say that the reused powder still has low coercively and its flowability is not compromised.

The flux rate index of virgin and reused powder was similar and very close to 1, which indicates that the powder is insensitive to flow variation, having not experienced energy changes in its displacement[28]. Similarly, the comparable stabilization index values found for the virgin and reused powder indicate that the powder did not undergo a sufficiently high transformation level, in terms of size and morphology, to the point of altering the powder stability. Aeration test results close to 1 indicate that the powder is not susceptible to aeration (AR<2)[28]. Thus, it is possible to infer that both powders behaved comparably even under a test setup with airflow addition.

Based on the rheological results obtained, it is possible to infer that reuse increased the energy required to provide displacement, that is, it affected the powder flowability. However, in terms of flow form load, stability, and aeration sensitivity, no appreciable differences were observed. This indicates that the current degradation level of the reused powder does not prevent its use[27,29].

3.3. Microstructure of the Inconel 625 parts manufactured by L-DED with virgin and reused powders

In Figure 9a, firstly, the absence of harmful defects, such as cracks and lack of fusion, stands out. It is worth mentioning that the presence of many chemical components with varying melting points in Inconel 625 promotes hot crack formation, making the alloy highly vulnerable to this phenomenon. Hence, considering the fast and out-of-equilibrium cooling conditions, laser processing windows free from this defect often are rather small[1]. This aspect indicates that the optimized L-DED parameter set used in this work was robust. Furthermore, it is possible to observe the molten pool boundaries characteristic of layer-by-layer additive manufacturing by the L-DED process. Observing the middle region of a molten pool in Figure 9b, it is interesting to note the microstructure heterogeneity, with dendritic grains that grow from the molten pool boundaries towards the center of the bead, in the opposite direction to the heat flow. These features can be linked to the fast cooling imposed by the laser and multiple heating/cooling cycles, which tend to provide a tempering effect between passes, and the formation of grains that cross multiple molten pool boundaries during solidification.

Grains in the middle of the molten pool seen in Figure 9b showed a more refined, polygonal shape. Magnified images of these regions are shown in Figure 9c and 9d. To allow for a direct microstructure comparison between the samples with such a heterogeneous solidification structure, microstructure analyses were carried out in this polygonal grain region. Microstructure was found to be composed of a dendritic Ni-rich matrix (light) with precipitates along the interdendritic regions (dark), which agrees with the microstructure reported for this material manufactured under similar processing conditions[30,31]. Quantitative image analysis of samples processed with virgin and reused powders indicated a precipitate content, in area %, of about 8.8% and 7.7%, respectively. Analysis of variance (ANOVA) and Tukey test revealed that the means were not significantly different at a significance level of 95%.

EDS spot ID analysis was performed at the dendritic (dark gray), interdendritic (light gray) and the precipitates region shown in Figure 10a. The chemical composition results are shown in Figure 10b, which indicates that Mo and Nb partitioned from the dendritic to the interdendritic region, where Mo and Nb-rich precipitates formed. This agrees with the solidification mechanism predicted by the Mo-Ni[32,] and Nb-Ni[33,] phase diagrams reported by Okimoto, where low solidification temperature eutectic points are expected to form. Surprisingly, although Nb and Mo are refractory metals with high melting points (2469 and 2623°C, respectively) when alloyed to Ni (with a melting point of 1455°C), Mo additions up to 47.7wt% decrease the liquid melting point to values as low as 1309°C. Similarly, Nb additions up to 23.5wt% and 51.9wt% decrease it even further to values around 1282 and 1175 °C, respectively. This way, considering that the Inconel 625 alloy contains about 8wt% Mo and 5wt% Nb (Table 1), it makes sense that Ni-rich clusters would solidify first at the dendritic regions, while Mo- and Nb-rich clusters remained liquid at the interdendritic regions, solidifying at lower temperatures. It is important to mention that the sample's thermal history also has an impact on the formation of these precipitates. In the as-built condition (before heat treatment) samples were found to have only approximately 3% of precipitate (in area%), as assessed by optical microscopy image quantification. As mentioned in the previous paragraph, after heat-treatment, the number of precipitates increased to about 8%, mainly located at interdendritic regions and grain boundaries.

Figure 11 shows higher magnification SEM images captured by SE and BSE modes, and EDS mapping of the sample processed with the reused powder. According to literature, Mo, Nb, and Si-rich precipitates refer to the Laves phases, which consist of intermetallic of brittle nature that typically occur in Inconel alloys[34,35]. Figure 11 also accuses the presence of abundant microparticles of Si and Mn-rich

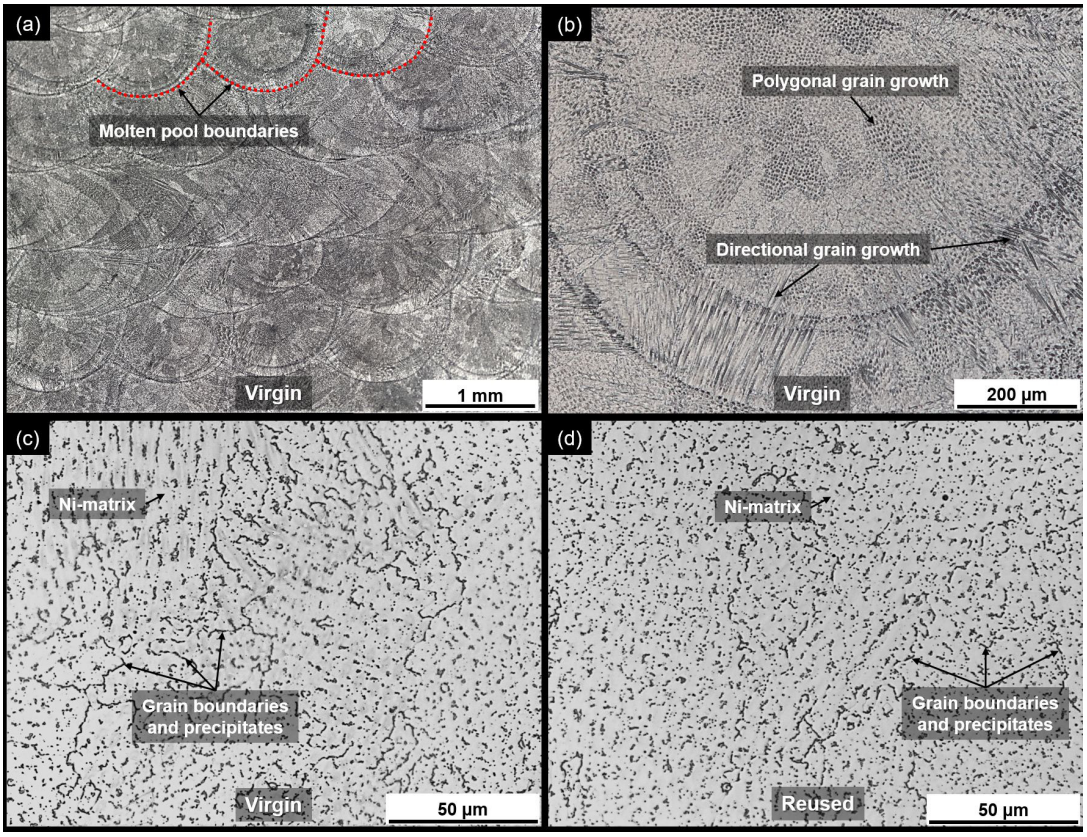

Figure 9. Macro and microscopic aspect of Inconel 625 powders processed by L-DED additive manufacturing after heat-treatment (900°C for 2 h), highlighting a (a) typical defect-free cross-section with (b) a magnified microstructure of a single bead showing directional solidification near the molten pool boundaries and polygonal grain solidification in the middle of the single bead. Magnified images of the polygonal grain region of samples processed with (c) virgin and (d) reused powders showing a Ni-rich dendritic matrix (light) with precipitates (dark) at grain boundaries and interdendritic regions.

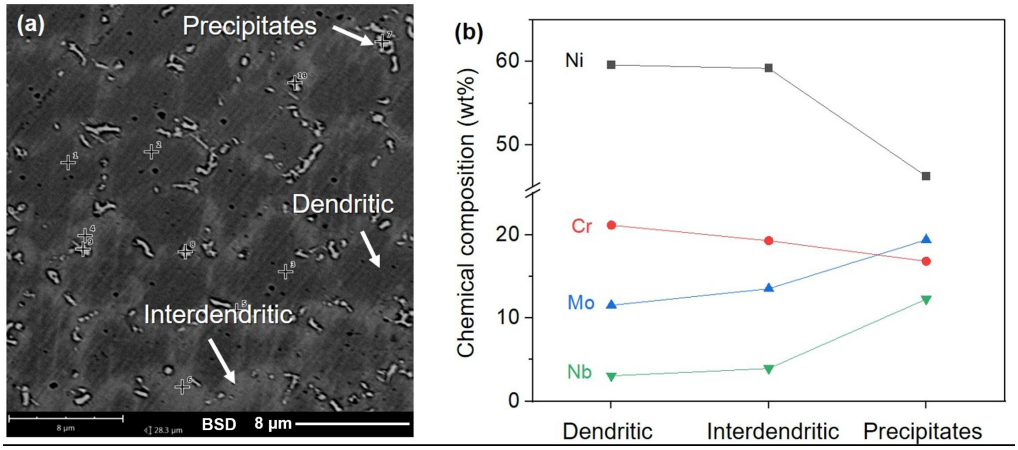

Figure 10. SEM image highlighting the (a) microstructure aspects, and (b) chemical composition analysis in the dendritic (dark gray), interdendritic (light gray), and the precipitates region showing the partition of Nb and Mo to the interdendritic region, where Nb and Mo-rich Laves phases precipitated.

oxides. These elements (Si and Mn) are present in the feedstock in trace amounts (<0.5wt%) and have great affinity for oxygen, often being used as deoxidizers in welding flux[36]. Although less frequently found, some Cr-oxide particles were also observed and have been reported to form during the processing of Inconel 625 alloy as CrO_2[37]. It is known

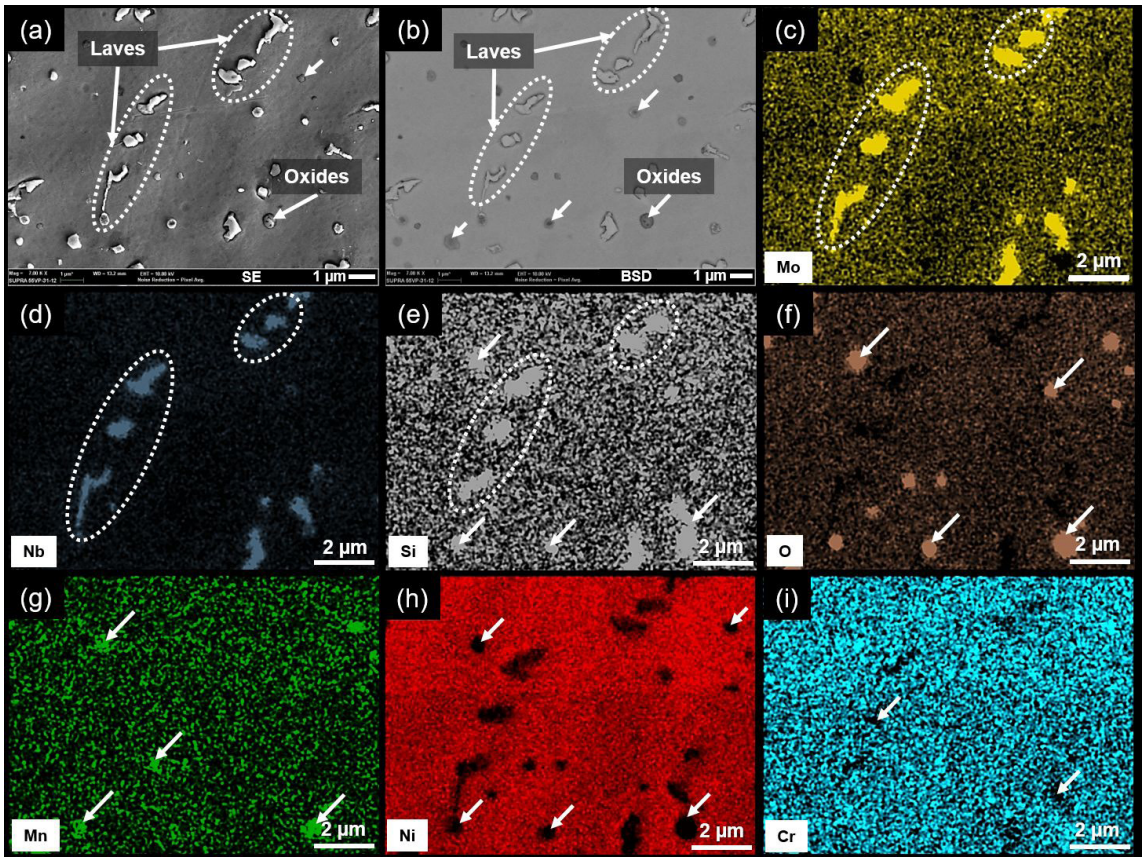

Figure 11. SEM images of Inconel 625 reused sample in the (a) SE, and (b) BSE mode. EDS indicates the presence of Laves phase with high-contents of (c) Mo, (d) Nb, and (e) Si, as well as oxides rich in (f) O, (g) Mn, and (e) Si. Some points with depletion of (h) Ni, and (h) Cr, are possibly related to the formation of pites.

that the passive layer developed on the surface of Inconel 625 alloys is predominantly composed of a compact and adherent Cr_2O_3 film[38-42]. This has been reported for Inconel 625 processed by different techniques such as L-DED[38], thermal spray[39], and L-PBF[40-42]. In samples processed by L-DED, a Mo oxide (MoO_2) was also detected in certain areas[38]. In samples processed by L-PBF, the surface of the material also showed the presence of Ni oxides, Ni-Cr oxides, and Ni-Fe oxides, such as NiO[40], NiO_2[41], $NiCr_2O_4$[40,42], $NiCrO_4$[41], and $NiFe_2O_4$[40,42]. In the present work, the source of oxygen might include pre-existing oxide contaminants in the feedstock (such as the ones seen in Figure 7 and 8) as well as trace contents of oxygen in the industrial argon gas used. The formation of these compounds is commonly mentioned in the literature[43,44]. Although MC-type carbides have been reported to form in this material[35], no significant amount of such particles has been found in the samples of this work, likely due to the very low C-content of the alloy, as shown in Table 1.

Figure 12 shows BSE images representative of the microstructure of samples processed with virgin (Figure 12a) and reused (Figure 12b) powder and highlights the significantly higher amount of oxides seen in samples deposited with the reused powder. In this sample, oxides have larger diameters and were found frequently in all examined locations. Oxides seem to be well distributed in the samples and are predominantly placed on the Ni-matrix, and not in interdendritic regions. This suggests that oxides may readily form during processing and act as a solid interface around which solidification starts. This could account for some degree of microstructure refinements, such as those observed in Figures 9c and 9d, but this hypothesis still requires further examination. Most important for this study, is the removal of corrosion-resistant elements from solid solution, which could impact the material's performance, as will be discussed in the following section.

3.4. Impact of feedstock reuse of the corrosion resistance

The cyclic polarization curves recorded for each condition and their corresponding replicas are shown in Figure 13. Results indicated that both conditions were able to passivate in the testing solution, as seen by the clear passivation region. For both conditions, the onset of pitting occurred at similar pitting potentials, which quickly recovered on scan reversion, leading to a more noble repassivation potential of about +600 mV. Nevertheless, the corrosion potential of samples processed with virgin powders was slightly more noble than that of samples processed with reused powders.

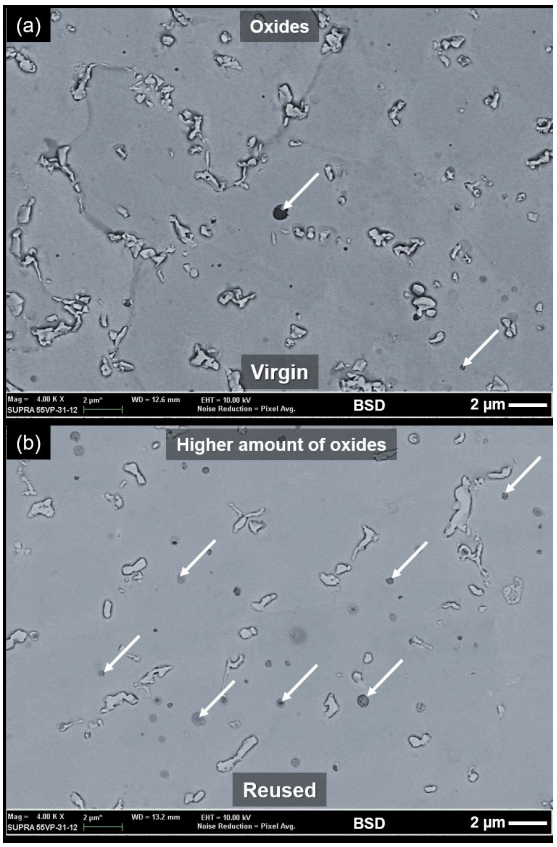

Figure 12. SEM images of Inconel 625 samples manufactured with (a) virgin and (b) reused powder, highlighting the significantly higher amount of oxides in the sample processed with reused powder.

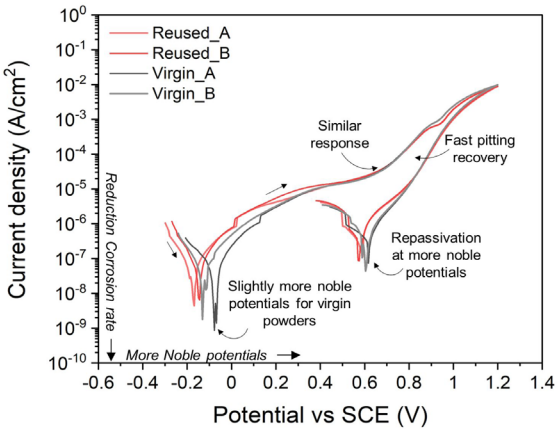

Figure 13. Cyclic voltammetry of Inconel 625 specimens processed by AM L-DED with virgin, and reused powder showing similar responses, with fast pitting recovery and repassivation at more noble potentials, but slightly more noble corrosion potentials for specimens manufactured with virgin powder.

The parameters derived from the Tafel analysis are summarized in Table 4 and illustrated in Figure 14. Specimens processed with virgin powders showed less variation in

Table 4. Tafel parameters of Inconel 625 specimens processed by L-DED with virgin and reused powders tested in NaCl 3.5% solution.

Specimen	Ecorr (mV)	Icorr (µA/cm²)	Rp (Ohm×cm²)
Virgin_A	-94	0.023	820
Virgin_B	-121	0.037	437
Mean ± SD	-108 ± 19	0.03 ± 0.01	628.5 ± 271
Reused_A	-176	0.036	407
Reused_B	-150	0.033	286
Mean ± SD	-163 ± 18	0.035 ± 0.002	346.5 ± 86

corrosion potential (E_{corr}), which was about 60 mV more positive than the specimens processed with reused powders. The polarization resistance (R_p) of specimens processed with virgin powder was also higher. Still, the corrosion rates (I_{corr}) of specimens processed with virgin and reused powder were not significantly different, being approximately 0.03 µA/cm².

OM analysis of the corroded surface, which was initially polished, resembled that of an etched surface, where the dendritic structure as well as the grain boundaries could be seen, as shown in Figure 15a and 15b, which suggest a certain degree of generalized corrosion. Still, the pitting corrosion mechanism was activated, as expected based on the curves of Figure 13 (for higher over potentials). Although no significant differences were recorded by cyclic polarization in terms of pitting resistance, OM analysis of the specimens after the corrosion test suggests that pitting corrosion was more developed in specimens processed with reused powder. Also, higher magnification optical microscopy analysis shown in Figure 15c revealed that pits were preferentially located in the dendritic regions.

To further examine the underlying causes of the observed differences, factors such as the fraction of precipitates, oxidation degree, microstructure refinement, and passive film features were considered, and are discussed as follows.

Investigation of the fraction of second phase is important because it may lead to Mo removal from solid solution for the formation of Mo-rich Laves phase precipitate. As Mo is known to impart pitting corrosion resistance in stainless steel[43] and Ni-based alloys[44], different amounts of precipitate could lead to different corrosion resistances. This agrees with the higher magnification optical microscopy analysis shown in Figure 15c, that reveals that the pits were preferentially located in the dendritic regions, where the Mo-content was decreased.

Quantitative microscopy analysis revealed that the sample processed with virgin powder had about 8.8±2.0% of second phase *versus* 7.7±1.0% of second phase in samples processed with reused powder, in area percentage. An example of the images used in these quantifications is seen in Figure 9c and Figure 9d, which represent a typical microstructure found in the middle of the molten pool (polygonal grain region). ANOVA and Tukey test, however, showed that the means are not significantly different from one another. In this context, results suggest that the reuse did not significantly affect the fraction of precipitates, not being a significant factor driving the observed differences.

High magnification SEM analysis revealed that samples showed differences in terms of oxidation, with

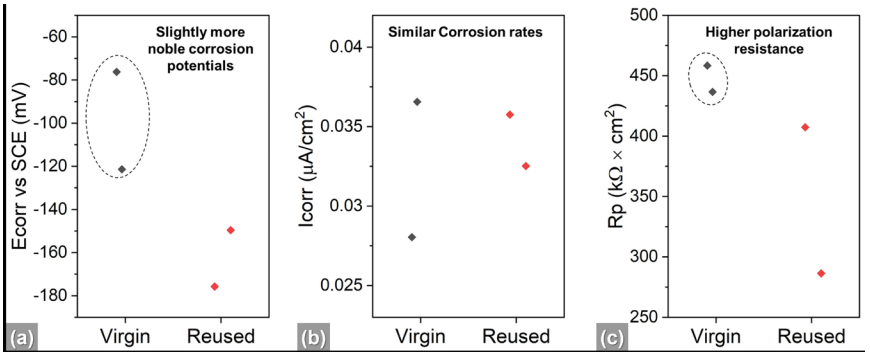

Figure 14. Summary of (a) corrosion potential, E_{corr} (b) corrosion current density, $I_{corr,}$ and (c) polarization resistance of Inconel 625 specimens processed by L-DED with virgin and reused powders, and tested in NaCl 3.5% solution.

the samples processed with reused powder showing larger oxide particles, as seen in Figure 11. The formation of larger oxide particles may be associated with the higher heat input and O_2 exposure that the reused feedstock went through in its processing history. As mentioned earlier, pre-existing feedstock impurities, residual O_2 present in the industrial-grade argon (used in processing), and exposure to an oxidizing atmosphere during the powder handling steps may be sources for oxidation. Another interesting point to notice is the chemical composition of oxides. Pre-existing oxides found in the feedstock were mostly composed of Al and Si elements, as seen in Figure 7 and Figure 8. In the L-DED processed samples, however, O_2 combined with the alloying elements to form Mn-, Si- and Cr-rich oxides. This is illustrated in Figure 11, where the formation of Si and Mn-oxides can be seen. Also, the higher content of oxides in the specimen processed with the reused alloy could be accounting for some degree of galvanic corrosion that could lead to a more accentuated pitting corrosion, as seen in Figure 15b.

Electrochemical impedance spectroscopy analysis indicates important differences in the passive film of each sample that could also be contributing to the observed differences. Figure 16 shows the (a,b) Bode, (c) Nyquist and (d)-Zim versus frequency plots recorded for the samples processed with virgin and reused powders. Measurements were found to be characteristic of a single time-constant[45]. For this reason, the Randles equivalent circuit was selected to fit the experimental data, which is consistent with other reports from literature[46,47].

Table 5 shows the EIS parameters derived from fitting to the Randles equivalent electrical circuit shown in Figure 16c. In this circuit, R_s represents the solution resistance, R_{ct} the charge transfer resistance to ions passing through the passive film, and CPE_{dl} the double layer capacitance, represented by a constant phase element with "n" exponent varying from n=0 (purely resistive) to n=1 (purely capacitive).

In Figure 16, samples show a high degree of capacitive behavior, as the n-exponent values were found to be 0.87 and 0.93. The slightly higher fraction of capacitive behavior seen for the processed with the reused powder could be associated with the higher content of oxides of these samples. The sample processed with virgin powder developed a smaller

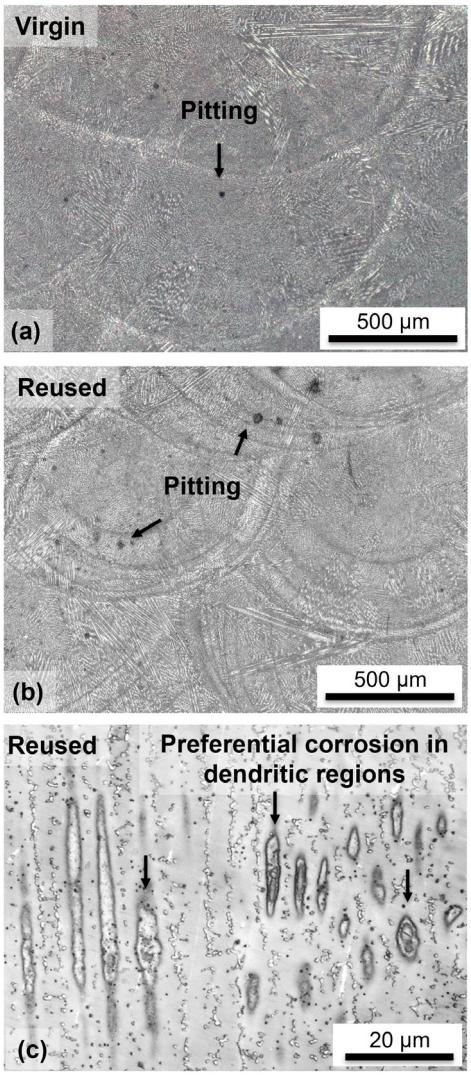

Figure 15. Microscopic aspect of the polished specimens processed with (a) virgin and (b) reused powder at the end of the corrosion test. Specimens developed an etched-like aspect, indicative of a certain degree of generalized corrosion after polarization, and (c) in both specimens, preferential pitting corrosion was found to occur in the dendritic regions where the Mo-content is much reduced.

Table 5. Electrochemical impedance spectroscopy parameters of Inconel 625 specimens processed by L-DED with virgin and reused powders in NaCl 3.5% solution, showing slightly higher charge transfer resistance and lower CPE values for samples processed with virgin powder.

Electrochemical Impedance Spectroscopy Parameters					
Powder	R_s ($\Omega \times cm^2$)	CPE ($\Omega^{-1} \times cm^{-2} \times s^n$)	n	R_{ct} ($\Omega \times cm^2$)	X^2
Virgin	14.6 ± 0.1	$2.2 \times 10^{-6} \pm 4.8 \times 10^{-8}$	0.87	$3.3 \times 10^5 \pm 3.0 \times 10^4$	2.99×10^{-4}
Reused	15.6 ± 0.2	$6.7 \times 10^{-6} \pm 2.5 \times 10^{-7}$	0.93	$1.6 \times 10^5 \pm 2.0 \times 10^4$	9.60×10^{-4}

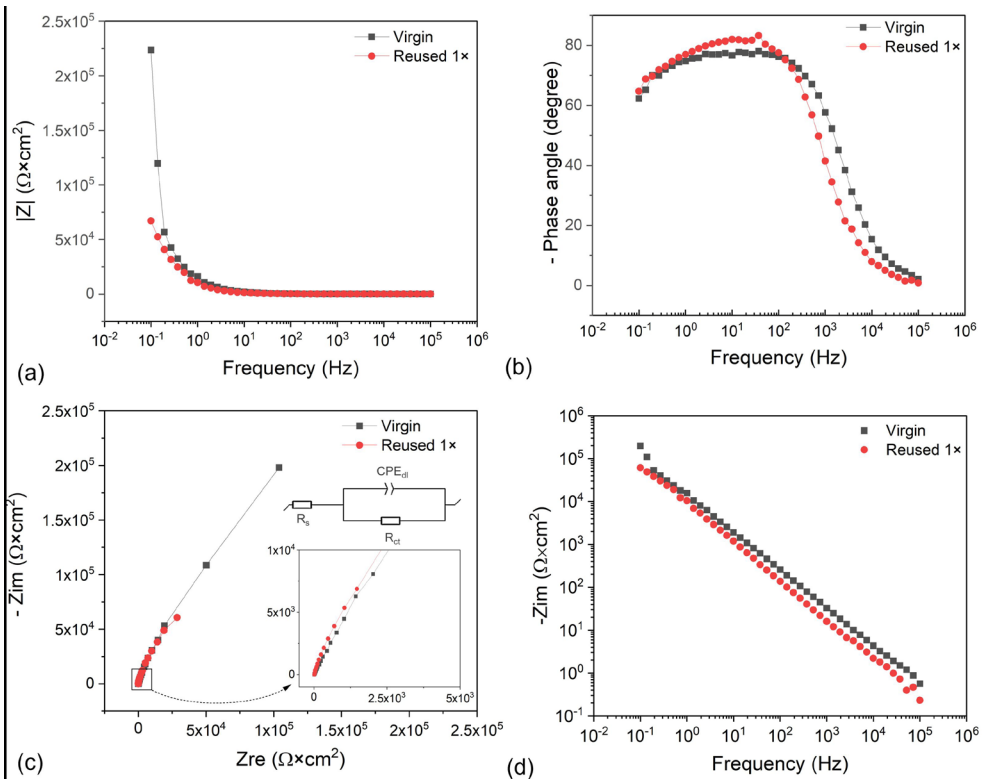

Figure 16. (a) Impedance, (b) phase angles (c) Nyquist and (d) -Zim versus Frequency graphs with both specimens showing data distribution characteristic of a single time. Specimens processed with virgin powder developed higher impedance values and a broader phase angle for higher frequencies, when tested in NaCl 3.5% solution, indicating a higher corrosion resistance.

CPE value, which is associated with the shift/broadening of the phase angle towards higher frequencies, indicating that a greater phase lag (between the input voltage and output current) is observed earlier in the experiment, i.e. for higher frequencies. In both plots, Figure 16a and Figure 16c, the higher impedance of the samples processed with virgin powder is evident. Also, the impedance fit analysis shows that the charge transfer resistance of the samples processed with virgin powder is over two times higher than that of the reused powders, which could be associated with a denser and/or thicker passive layer. It is important to highlight that section 3.3 detailed the primary categories of oxides reported in the literature as well as the oxides identified in this work, including the passive layer of Cr_2O_3 and Mn and Si-rich oxides (contaminations present in the powder, inert gas or inserted at any stage of powder handling). According to Gullapudi, a more refined structure is expected to form a denser passive film[48]. The higher heat-input the reused powder was exposed to could also result in some degree of microstructure coarsening. This is corroborated by Figure 5 results that suggest that a more refined microstructure has a higher corrosion resistance.

Although powder reused was found to have an impact on the corrosion resistance of Inconel 625 alloys manufactured by L-DED, the observed differences are subtle and may not be as significant as the effect of other laser processing parameters[49] or other processing techniques[48]. Therefore, results confirm that the reuse of Inconel 625 powder processed under argon-gas controlled conditions has no significant detrimental impact of the corrosion resistance in NaCl 3.5% media, being a cost effective way of increasing the competitiveness of additive manufacturing parts. For future studies, investigation of the corrosion performance of the samples in the as-built versus heat-treated condition is also of interest.

For future studies, further investigation of the intricacies of the oxides formed on the surface of Inconel 625 processed by L-DED by XPS is suggested. Although some studies addressing the formation of oxides in Inconel 625 processed by L-PBF are found in literature[40-42], studies on the response of samples processed by L-DED are still scarce, and knowledge may not be fully extrapolated as metallurgical differences associated with the particle size and higher cooling rates could lead to different formation mechanism or kinetics. This would contribute to a better understanding on how multiple reuses impact the passive film formation. The investigation of the corrosion resistance for more cycles of reuse is also greatly encouraged, as a contribution towards the culture of sustainable manufacturing.

4. Conclusions

Inconel 625 samples were processed by AM L-DED using virgin and reused powder (after 1 cycle of reuse). The microstructure was characterized by optical and scanning electron microscopy, the chemical composition by EDS, and the corrosion performance by cyclic polarization and EIS analysis carried out in naturally aerated 3.5% NaCl solution. The following conclusions were reached:

- Except for a slight decrease in powder flowability of the reused powder (that required more energy), no significant differences were detected between the virgin and reused powder.
- Processed samples showed columnar dendritic microstructure with the formation of Mo- and Nb-rich Laves phase precipitates at grain boundaries that are partitioned to the interdendritic region. Similar amounts of second phase precipitated were observed in both samples. Samples presented generalized and pitting corrosion mechanisms, with the latter being preferentially located at the Mo-depleted dendritic region.
- Although specimens processed with virgin powder had slightly higher corrosion potential and polarization resistance than samples processed with reused powder, both sample conditions showed very similar polarization curves with a clear passivation plateau and repassivation at more positive potentials.
- Samples processed with reused powder were found to have a high content of Si, Mn, and Cr oxides, which accounted for a slightly inferior impedance and charge transfer resistance. Although cyclic polarization curves did not indicate a significant difference in the pitting behavior, optical microscopy analysis of the corroded surfaces suggests that specimens processed with reused power could be slightly more susceptible to pitting corrosion mechanisms.

5. Acknowledgments

Authors gratefully acknowledge the Agência Nacional de Petróleo, Gás Natural e Biocombustíveis (ANP) and the Empresa Brasileira de Pesquisa e Inovação Industrial (EMBRAPII) for RD&I funding in the scope of the Digital Additive Manufacturing project. Authors would also like to thank, SENAI Innovation Institute in Manufacturing Systems and Laser Processing, and the Laboratory of Biomaterials and Electrochemistry of the Federal University of Paraná for providing laboratory infrastructure, materials, and technical support. Research funding from the Conselho Nacional de Desenvolvimento Científico e Tecnológico (CNPq), process number 302144/2022-6, is gratefully acknowledged.

6. References

1. Lu N, Lei Z, Hu K, Yu X, Li P, Bi J, et al. Hot cracking behavior and mechanism of a third-generation Ni-based single-crystal superalloy during directed energy deposition. Addit Manuf. 2020;34:101228. http://doi.org/10.1016/j.addma.2020.101228.
2. Hu Y, Li Y, Fan W, Gao X, Zhang Q, Wang Q, et al. Hot workability and microstructural evolution of a nickel-based superalloy fabricated by laser-based directed energy deposition. J Alloys Compd. 2022;920:165373. http://doi.org/10.1016/j.jallcom.2022.165373.
3. Nguejio J, Szmytka F, Hallais S, Tanguy A, Nardone S, Godino Martinez M. Comparison of microstructure features and mechanical properties for additive manufactured and wrought nickel alloys 625. Mater Sci Eng A. 2019;764:138214. http://doi.org/10.1016/j.msea.2019.138214
4. Dutkiewicz J, Rogal L, Kalita D, Berent K, Antoszewski B, Danielewski H, et al. Microstructure and properties of Inconel 625 fabricated using two types of laser metal deposition. Materials. 2020;13(21):1-17. http://doi.org/10.3390/ma13215050.
5. Fei J, Liu G, Patel K, Özel T. Effects of machining parameters on finishing additively manufactured nickel-based alloy Inconel 625. Manuf Mater Processi. 2020;4(2):32. http://doi.org/10.3390/jmmp4020032.
6. Barragan G, Rojas Perilla DA, Grass Nuñez J, Mariani F, Coelho R. Characterization and optimization of process parameters for directed energy deposition powder-fed laser system. J Mater Eng Perform. 2021;30(7):5297-306. http://doi.org/10.1007/s11665-021-05762-9.
7. ASTM: American Society for Testing and Materials. ASTM F3187: standard guide for directed energy deposition of metals [Internet]. West Conshohocken: ASTM; 2016. p. 1-22 [cited 2023 Dec 29]. Available from: https://www.astm.org/f3187-16.html
8. Sangali M, Cremasco A, Soyama J, Caram R, Contieri RJ. Selective laser melting of Ti-6Al-4V: correlation between processing parameters, microstructure and corrosion properties. Mater Res. 2023;26(Suppl suppl 1):e20230055. http://doi.org/10.1590/1980-5373-mr-2023-0055.
9. Gan M, Wu Q, Long L. Prediction of residual deformation and stress of laser powder bed fusion manufactured Ti-6Al-4V lattice structures based on inherent strain method. Mater Res. 2023;26:e20220516. http://doi.org/10.1590/1980-5373-mr-2022-0516.
10. Gradl P, Tinker DC, Park A, Mireles OR, Garcia M, Wilkerson R, et al. Robust metal additive manufacturing process selection and development for aerospace components. J Mater Eng Perform. 2022;31(8):6013-44. http://doi.org/10.1007/s11665-022-06850-0.
11. Sui S, Chen J, Fan E, Yang H, Lin X, Huang W. The influence of Laves phases on the high-cycle fatigue behavior of laser additive manufacturing Inconel 718. Mater Sci Eng A. 2017;695:6-13. http://doi.org/10.1016/j.msea.2017.03.098.
12. Volpato GM, Tetzlaff U, Fredel MC. A comprehensive literature review on laser powder bed fusion Inconel superalloys. Addit Manuf. 2022;55:102871. http://doi.org/10.1016/j.addma.2022.102871.
13. Ramkumar KD, Abraham WS, Viyash V, Arivazhagan N, Rabel AM. Investigations on the microstructure, tensile strength and high temperature corrosion behaviour of Inconel 625 and Inconel 718 dissimilar joints. J Manuf Process. 2017;25:306-22. http://doi.org/10.1016/j.jmapro.2016.12.018.

14. Kumar SP, Elangovan S, Mohanraj SE, Ramakrishna JR. A review on properties of Inconel 625 and Inconel 718 fabricated using direct energy deposition. Mater Today Proc. 2021;46:7892-906. http://doi.org/10.1016/j.matpr.2021.02.566.
15. Verdi D, Varadaraju N, Tan Zhi'En E, Patran A. Effect of manufacturing strategy on the toughness behavior of Inconel 625 laser metal deposited parts. Adv Eng Mater. 2022;23(7):2001506. http://doi.org/10.1002/adem.202001506.
16. Alfaify A, Saleh M, Abdullah FM, Al-Ahmari AM. Design for additive manufacturing: a systematic review. Sustainability. 2020;12(19):1-22. http://doi.org/10.3390/su12197936.
17. Gutjahr J. Efeitos da reutilização do pó metálico no processo Laser Directed Energy Deposition (L-DED): uma análise sobre a degradação da matéria-prima e suas consequências no processo e no comportamento de peças fabricadas por manufatura aditiva [thesis]. Florianópolis: Universidade Federal de Santa Catarina; 2022.
18. Renderos M, Torregaray A, Gutierrez-Orrantia ME, Lamikiz A, Saintier N, Girot F. Microstructure characterization of recycled IN718 powder and resulting laser clad material. Mater Charact. 2017;134:103-13. http://doi.org/10.1016/j.matchar.2017.09.029.
19. Slotwinski JA, Garboczi EJ, Stutzman PE, Ferraris CF, Watson SS, Peltz MA. Characterization of metal powders used for additive manufacturing. J Res Natl Inst Stand Technol. 2014;119():460-93. http://doi.org/10.6028/jres.119.018.
20. Thiesen A Jr. Selection of processing parameters for the laser directed energy deposition process applied to additive manufaturing: a methodological proposal [dissertation]. Joinville: Universidade Federal de Santa Catarina; 2021.
21. ASTM: American Society for Testing and Materials. ASTM B215: standard practices for sampling metal powders. West Conshohocken: ASTM; 2020. p. 1-7. http://doi.org/10.1520/B0215-20.
22. ASTM: American Society for Testing and Materials. ASTM G3: standard practice for conventions applicable to electrochemical measurements in corrosion testing. West Conshohocken: ASTM; 2019. p. 1-9. http://doi.org/10.1520/G0003-14R19.
23. Terrassa KL, Haley JC, MacDonald BE, Schoenung JM. Reuse of powder feedstock for directed energy deposition. Powder Technol. 2018;338:819-29. http://doi.org/10.1016/j.powtec.2018.07.065.
24. Sindo K. Welding metallurgy. New Jersey: John Wiley & Sons; 2003.
25. Leturia M, Benali M, Lagarde S, Ronga I, Saleh K. Characterization of flow properties of cohesive powders: a comparative study of traditional and new testing methods. Powder Technol. 2014;253:406-23. http://doi.org/10.1016/j.powtec.2013.11.045.
26. Sutton AT, Kriewall CS, Karnati S, Leu MC, Newkirk JW. Characterization of AISI 304L stainless steel powder recycled in the laser powder-bed fusion process. Addit Manuf. 2020;32:100981. http://doi.org/10.1016/j.addma.2019.100981.
27. Gutjahr J, Pereira M, Sousa JMSS, Ferreira HS, Thiesen A Jr. Powder degradation interaction: a study of SS 316L powder reuse on the laser directed energy deposition process. J Laser Appl. 2024;36:012022. http://doi.org/10.2351/7.0001093.
28. Freeman R. Measuring the flow properties of consolidated, conditioned and aerated powders - A comparative study using a powder rheometer and a rotational shear cell. Powder Technol. 2007;174(1-2):25-33. http://doi.org/10.1016/j.powtec.2006.10.016.
29. Dawes BJ, Bowerman R, Trepleton R. Introduction to the Additive Manufacturing Powder Metallurgy Supply Chain: exploring the production and supply of metal powders for AM processes. Johnson Matthey Technology Review. 2015;59(3):243-56. http://doi.org/10.1595/205651315X688686.
30. Mehrabi O, Seyedkashi SMH, Moradi M. Functionally graded additive manufacturing of thin-walled 316L stainless steel-Inconel 625 by direct laser metal deposition process: characterization and evaluation. Metals. 2023;13(6):1-18. http://doi.org/10.3390/met13061108.
31. Danielewski H, Antoszewski B. Microstructure and properties of laser additive deposited of nickel base super alloy Inconel 625. De Gruyter. 2020;10:484-90. http://doi.org/10.24425/afe.2020.133330.
32. Okamoto H. Nb-Ni (Niobium-Nickel). J Phase Equilibria. 1998;19(3):289. http://doi.org/10.1361/105497198770342508.
33. Okamoto H. Mo-Ni (Molybdenum-Nickel). J Phase Equilibria. 1991;12(6):703. http://doi.org/10.1007/BF02645183.
34. Wang X, Chen C, Qin L, Zhang M. Microstructure evolution and mechanical behavior of Inconel 625 produced using direct laser metal deposition. Phys Met Metallogr. 2021;122(9):896-907. http://doi.org/10.1134/S0031918X2109012X.
35. Zhong C, Ren X, Fu K, Luan B. Effect of thermal aging on the microstructure and mechanical properties of Inconel 625 superalloy fabricated by high-speed laser metal deposition. Metall Mater Trans, B, Process Metall Mater Proc Sci. 2023;54B(5):2723-36. http://doi.org/10.1007/s11663-023-02869-3.
36. Kozyrev NA, Kryukov RE, Lipatova UI, Kozyreva OE. On the use of slag from silicomanganese production for welding flux manufacturing. IOP Conf Series Mater Sci Eng. 2016;150:1-9. http://doi.org/10.1088/1757-899X/150/1/012032.
37. Marchese G, Garmendia Colera X, Calignano F, Lorusso M, Biamino S, Minetola P, et al. Characterization and comparison of Inconel 625 processed by selective laser melting and laser metal deposition. Adv Eng Mater. 2017;19(3):1-9. http://doi.org/10.1002/adem.201600635.
38. Zhang W, Xu Y, Shi Y, Su G, Gu Y, Volodymyr K. Intergranular corrosion characteristics of high-efficiency wire laser additive manufactured Inconel 625 alloys. Corros Sci. 2022;205:110422. http://doi.org/10.1016/j.corsci.2022.110422.
39. Chen T-C, Chou CC, Yung T-Y, Cai R-F, Huang J-Y, Yang Y-C. A comparative study on the tribological behavior of various thermally sprayed Inconel 625 coatings in a saline solutions and deionized water. Surf Coat Tech. 2020;385:125442. http://doi.org/10.1016/j.surfcoat.2020.125442.
40. Chen L, Sun Y, Li L, Ren X. Effect of heat treatment on the microstructure and high temperature oxidation behavior of TiC/Inconel 625 nanocomposites fabricated by selective laser melting. Corros Sci. 2020;169:108606. http://doi.org/10.1016/j.corsci.2020.108606.
41. Parizia S, Marchese G, Rashidi M, Lorusso M, Hryha E, Manfredi D, et al. Effect of heat treatment on microstructure and oxidation properties of Inconel 625 processed by LPBF. J Alloys Compd. 2020;846:156418. http://doi.org/10.1016/j.jallcom.2020.156418.
42. Sun Y, Chen L, Li L, Ren X. High-temperature oxidation behavior and mechanism of Inconel 625 super-alloy fabricated by selective laser melting. Opt Laser Technol. 2020;132:106509. http://doi.org/10.1016/j.optlastec.2020.106509.
43. Ha H-Y, Lee T-H, Bae J-H, Chun DW. Molybdenum effects on pitting corrosion resistance of FeCrMnMoNC austenitic stainless steels. Metals. 2018;8(8):1-13. http://doi.org/10.3390/met8080653.
44. Ilevbare GO, Burstein GT. The role of alloyed molybdenum in the inhibition of pitting corrosion in stainless steels. Corros Sci. 2001;43(3):485-513. http://doi.org/10.1016/S0010-938X(00)00086-X.
45. Hirschorn B, Orazem ME, Tribollet B, Vivier V, Frateur I, Musiani M. Constant phase element behavior caused by resistivity distributions in films II. Aplications. J Electrochem Soc. 2010;12(12):C458-63. http://doi.org/10.1149/1.3499565.
46. Jeyaprakash N, Yang CH, Karuppasamy SS, Dhineshkumar SR. Evaluation of microstructure, nanoindentation and corrosion behavior of laser cladded Stellite-6 alloy on Inconel-625 substrate. Mater Today Commun. 2022;31:103370. http://doi.org/10.1016/j.mtcomm.2022.103370.
47. Gui W, Zhong C, Gu J, Ding Y, Wang X, Wu T, et al. Laser-clad Inconel 625 coatings on Q245R structure steel: microstructure,

wear and corrosion resistance. npj Mater Degrad. 2022;37(1):1-11. http://doi.org/10.1038/s41529-022-00247-z.

48. Gollapudi S. Grain size distribution effects on the corrosion behavior of materials. Corros Sci. 2012;62:90-4. http://doi.org/10.1016/j.corsci.2012.04.040.
49. He K, Dong L, Wang Q, Zhang H, Li Y, Liu L, et al. Comparison on the microstructure and corrosion behavior of Inconel 625 cladding deposited by tungsten inert gas and cold metal transfer process. Surf Coat Tech. 2022;435:128245. http://doi.org/10.1016/j.surfcoat.2022.128245.